Molecular Simulation
Vol. 00, No. 00, Month 200x, 1–18

DRAFT - not submitted

A novel methodology to determine effective transport properties of fluids in nanoporous media by non-equilibrium molecular dynamics simulation

Hendrik Frentrup[a], Carlos Avendaño[b], Martin Horsch[c], Alaaeldin Salih[a], Erich A. Müller[a] *

[a] *Department of Chemical Engineering, Imperial College London, South Kensington Campus, London SW7 2AZ UK*;
[b] *School of Chemical and Biomolecular Engineering, Cornell University, 120 Olin Hall, Ithaca, New York 14853, USA*;
[c] *Lehrstuhl für Thermodynamik, Technische Universität Kaiserslautern, Erwin-Schrödinger-Str. 44, 67663 Kaiserslautern, Germany*

(*v0.1 received June 2011*)

This work presents the investigation of fluid transport through nanoporous materials through a novel, highly efficient Non-Equilibrium Molecular Dynamics (NEMD) methodology. The method allows for a distinction between diffusive and viscous contributions of the mass transport. Both pore and fluid particle interactions are represented by coarse-grained molecular models, in order to present a proof-of-concept and to retain computational efficiency in the simulations. A steady flow was induced by applying an external field to only a small region of the fluid. The external field constitutes a potential difference, mimicking a chemical potential gradient, which in turn triggers a diffusive flux through the membrane pores. The heat dissipated by the viscous flow is released by a Gaussian thermostat applied to the wall particles. The method is effective in studying planar Poiseuille flow in a slit pore as well as more natural, complex wall geometries. The dependence of the diffusive flux on the external field sheds light on the transport diffusivities and allows a direct calculation of effective diffusivities. The application of the method is demonstrated in two different test cases, namely the mass transport through a slit pore and the calculation of the effective self-diffusion through this system.

Keywords: non-equilibrium molecular dynamics; diffusion; Lennard-Jones potential; slit pore;

1 Introduction

Numerous types of nanoporous media found their way into membrane modules and chemical reactors for industrial use, among them zeolite structures and metal-organic frameworks. There is an abundance of applications for effective models in chemical and process engineering, as much as there is an anticipation of significant advances in progressive technologies, such as nanofiltration, gas separation, water purification, desalination, energy generation, fuel cell technology and many more.

Due to the complexity, the potentially high number of species involved, and discontinuities on the nanoscale, a rigorous thermodynamic treatment of microscopic mass transport continues to be a challenge in chemical engineering. For instance, the Hagen-Poiseuille equation allows an estimation of the required pressure to invoke a specific flux through the cylindrical pore [1]. However, mass transport through nanoporous media is governed by characteristics on the molecular level. It has been found that a classical treatment of fluid dynamics, namely the continuum Navier-Stokes equations, break down on the nanoscale [2]. Models of increasing complexity are

*Corresponding author. Email: e.muller@imperial.ac.uk

ISSN: 1351-847X print/ISSN 1466-4364 online

DOI: 10.1080/1351847YYxxxxxxxx
http://www.informaworld.com

being devised in an attempt to account for these phenomena [3]. The models fail to incorporate a full molecular character and a complete molecular treatment is still in development. As the access to powerful computational resources spreads, molecular simulation plays an increasingly important role in this development. Computer experiments help explore the limits of classical models and discoveries can sometimes be predicted by simulation and thereupon proven experimentally [4–7].

The aim of this work is to explore a novel approach to simulate mass transport in porous materials. After a brief evaluation of existing simulation techniques in the following section, enhancements of a suitable approach are proposed in section 3. The benefit of the approach is its simplicity, efficiency and its applicability to a wide range of conditions and systems. The method can be used to analyze the mobility of confined fluids, yielding a direct route to diffusivities. The methodology is applied to a model system and the results are presented in section 4.

2 Diffusion: Theory and Simulation

Mass transfer can principally attributed to two different mechanism: macroscopic transport via convection and microscopic transport from diffusion. In pores on the scale of a few nanometers in diameter, diffusion is the primary mechanism behind mass transport. Convective contributions can be considered small. There are several different theories to describe mass transport through diffusion. At the outset, the treatment with a clearly defined background in statistical mechanics will be introduced. Subsequently, a phenomenological approach, which is the basis for several simulation approaches, is presented. These simulation approaches are described alongside.

2.1 *Self-diffusion and collective diffusion*

In a bulk system of a pure substance at equilibrium, the self-diffusion is defined as a measure of the mobility of a single tagged particle in a bulk of otherwise identical particles. The corresponding transport property is the self-diffusion coefficient D_s [5, 8, 9]. Since random thermal motion of the particles is the source for self-diffusion, it highly depends on temperature and density of the system. The calculation of D_s within a molecular ensemble can be performed using the Einstein's relation or equivalently by using the Green-Kubo relations in terms of the velocity auto-correlation function (VACF):

$$D_\mathrm{s} = \frac{1}{2d} \lim_{t\to\infty} \frac{\mathrm{d}}{\mathrm{d}t} \left\langle \frac{1}{N_\mathrm{f}} \sum_{i=1}^{N_\mathrm{f}} |\mathbf{r}_i(t) - \mathbf{r}_i(0)|^2 \right\rangle = \frac{1}{d} \int_0^\infty \left\langle \frac{1}{N_\mathrm{f}} \sum_{i=1}^{N_\mathrm{f}} \mathbf{v}_i(t) \cdot \mathbf{v}_i(0) \right\rangle \mathrm{d}t \,, \tag{1}$$

where $\mathbf{r}_i(t)$ and $\mathbf{v}_i(t)$ are the position and velocity of particle i at time t, respectively, N_f is the number of particles, and d is the dimensionality of the system. In Eq. 1, the terms in the angular brackets denote an ensemble average, either of the particle's mean-square displacement (MSD) for the first expression on the right-hand-side, or of the VACF for the second expression. In a dense fluid, the MSD increases linearly with time due to frequent collisions of the particles [10]. After accounting for the dimensionality of the system, this linear relationship is the self-diffusivity, describing the mobility of the particles. The VACF, which has a strong foundation on statistical mechanics [11], originates from a generalized expression for transport properties.

The diffusion of a single tagged particle in a mixture of two different species is called *tracer diffusion*. The distinction is due to the fact that a tagged particle in a mixture will not only interact with particles of the same species but also with particles of a different species, implying that composition has an influence on the outcome. Apart from temperature and density, confinement can also have an influence on a substance's self-diffusivity by restricting its mobility.

In a mixture, the motion of one species is also correlated to the motion of the other species. Thus, the mobility of a particle becomes a collective property and the computation requires to take the velocity correlation function (VCF) of the entire system into account. Accordingly, the integration over this VCF yields the collective diffusivity D_c [12]:

$$D_\mathrm{c} = \frac{1}{d}\int_0^\infty \left\langle \frac{1}{N_\mathrm{f}} \sum_{j=1}^{N_\mathrm{f}} \mathbf{v}_j(t) \cdot \sum_{i=1}^{N_\mathrm{f}} \mathbf{v}_i(0) \right\rangle \mathrm{d}t \; . \tag{2}$$

It shall be noted that in eq. 2, there is an additional summation compared to Eq. 2, but the velocity auto-correlation function is still part of this summation. Therefore, the self-diffusivity and a cross contribution D_ξ constitute the collective diffusivity and $D_\mathrm{c} = D_\mathrm{c} + D_\xi$. For low density fluids, D_ξ is negligible and the collective diffusivity approaches the self-diffusivity [13].

2.1.1 Equilibrium Molecular Dynamics Simulations

Equilibrium Molecular Dynamics (EMD) simulations have been performed to analyze self-diffusivities of liquids since early 1980s [14]. It is the most traditional approach as the trajectories of the particles can be directly taken from the simulations and used in Eq. 1 and 2. Equilibrium MD methods are a common route to the self-diffusivity of a substance because simulation results can be compared to experimental measurements from pulsed-field gradient nuclear magnetic resonance and neutron scattering measurements [5]. Moreover, the calculation of self-diffusivities by EMD is convenient because the auto-correlation functions, or the mean-square displacement for that matter, converges very quickly, due to the possibility of averaging over all particles. In terms of the collective diffusivity, the correlation between a particle's velocity with all other particle velocities has to be determined and the correlations function converges very slowly [9]. Several extremely long simulations need to be performed to obtain viable results. To simulate collective diffusivities from EMD is very computationally expensive and therefore non-equilibrium approaches as a direct route to simulate transport phenomena have been pursued. A synopsis of these are given in section 2.2.1.

2.2 *Transport diffusion*

Transport diffusion occurs when a system is not at equilibrium and gradients in concentration, pressure or temperature cause a net mass flux. Similar to the self-diffusion, the magnitude of the diffusive flux, J^D, is governed by the mobility of the substance. In the presence of concentration gradients, i.e. under non-equilibrium conditions, the mass transport in the continuous system is commonly described by Fick's first law [15]:

$$\mathbf{J}^\mathrm{D} = -D_\mathrm{t}(\rho)\boldsymbol{\nabla}\rho \; , \tag{3}$$

where ρ denotes the fluid density and D_t is the coefficient of transport diffusion (also called Fickian diffusivity). In general, D_s and D_t are inherently different. For an infinitely diluted mixture of low density gases, the value for D_t, describing the transport diffusion of the solute, approaches the tracer diffusivity D_s [16]. Due to its simple formulation, the Fickian approach is wide-spread in engineering. However, the formulation breaks down for certain non-ideal cases. For instance, at the interface of two separate phases in equilibrium, a considerable gradient in concentration will not induce a net flux. In response, the perception of a gradient in chemical potential being the fundamental driving force of mass transport was conceived.

$$\mathbf{J}^\mathrm{D} = -L(\rho)\boldsymbol{\nabla}\mu \tag{4}$$

Here, the diffusive flux is related to a chemical potential gradient via a phenomenological transport coefficient L, called Onsager coefficient [17]. It is worth noting that mass transport in porous media deals with the porous material being stationary and a net flux occurs only for the confined fluid. When dealing with a pure confined fluid, the transport equations simplify significantly. Moreover, with a single component flowing through the porous structure, a density gradient must coincide with a pressure gradient. The aforementioned distinction between convective and diffusive contributions is necessary in the description of mass transport since convective flux, J^{C}, stems from macroscopic motion while the diffusive flux happens on a microscopic scale and occurs due to the random thermal motion of the molecules. Under the assumption that a convective mass flux is only provoked by a gradient in pressure [18], one-dimensional mass transport can be described by:

$$J^{\mathrm{total}} = J^{\mathrm{D}} + J^{\mathrm{C}} = -L\left(\frac{\partial \mu}{\partial x}\right) - \kappa_{\mathrm{c}}\left(\frac{\partial p}{\partial x}\right) \ , \tag{5}$$

where μ and p denote the chemical potential and pressure, respectively. κ_{c} denotes the linear phenomenological transport coefficients for convective mass transport. For a cylindrical pore on the macroscale, κ_{c} is a function of the pore radius R and the fluid viscosity η and density ρ, that is $\kappa_{\mathrm{c}} = \rho R^2/8\eta$ [12]. For a pore of only a few molecular diameter in width, this expression is not applicable, however. In a single-component system at constant temperature ($m = 1,\ \mathrm{d}T = 0$), the Gibbs-Duhem equation yields a direct relationship between the system's natural thermodynamic variables, namely the chemical potential and the pressure, as it reduces to $\mathrm{d}\mu = \mathrm{d}p/\rho$. This expression can be used to simplify Eq. 5, and one obtains:

$$J^{\mathrm{total}} = -\left[L + \kappa_{\mathrm{c}}\rho\right]\left(\frac{\partial \mu}{\partial x}\right) \ . \tag{6}$$

Given this expression, it is straightforward to redraft the Fickian approach into an equivalent Onsager expression by relating a gradient in chemical potential and density gradient via the thermodynamic correction factor Γ, also called *Darken* factor [9]:

$$\Gamma \equiv \frac{1}{k_{\mathrm{B}}T}\left(\frac{\partial \mu}{\partial \ln \rho}\right)_T \ . \tag{7}$$

When the chemical potential of a substance expressed in terms of the definition of fugacity f, $\mu/\mu_0 = k_{\mathrm{B}}T \ln f$, the thermodynamic factor can be expressed as $\Gamma = (\ln f/\ln \rho)_{_T}$. For a low density gas, the Darken factor approaches unity and therefore the transport diffusion coefficient approaches the self-diffusivity. This becomes evident when considering an ideal gas, for which $\mathrm{d}\mu = k_{\mathrm{B}}T \ln \rho$. It is convenient to express the flux equation in terms of a gradient in density and therefore Eq. 7 can be used in Eq. 6, which yields:

$$J^{\mathrm{total}} = -\underbrace{\left(D_0 + k_{\mathrm{B}}T\kappa_{\mathrm{c}}\right)\Gamma}_{\text{effective diffusivity } D_{\mathrm{eff}}}\left(\frac{\partial \rho}{\partial x}\right) \ . \tag{8}$$

while D_0 is being defined as $D_0 \equiv k_{\mathrm{B}}TL/\rho$. Equation 8 is of central importance for the application of the simulation approach in this study. In the limit of a vanishing difference in pressure, one can argue that the convective component of the mass transport, κ_{c}, is negligible. In this case, the effective diffusivity approaches the transport diffusivity and $D_{\mathrm{eff}} = D_0\Gamma = D_{\mathrm{t}}$. The aim of this study is to explore the possibilities to use molecular simulation for these limiting cases.

Similarly considering the chemical potential gradient as the driving force behind diffusion, the Maxwell-Stefan [1] description of diffusive mass transport for two-component bulk diffusion (under the assumption that the porous medium acts as a bulk component) can be expressed as:

$$-\boldsymbol{\nabla}\mu_1 = \frac{k_\mathrm{B}T}{Đ_\mathrm{MS}} x_2(\mathbf{u}_1 - \mathbf{u}_2) \; , \tag{9}$$

where $Đ_\mathrm{MS}$ denotes the Maxwell-Stefan diffusivity and $\mathbf{u}_i (i = 1, 2)$ are the average velocities of the fluid ($i = 1$) and the porous material ($i = 2$). The resistence to mix is influenced by the composition of the "mixture" and a frictional drag, expressed by the drag coefficient $k_\mathrm{B}T/Đ_\mathrm{MS}$. Since the definition of x_2 is not meaningful for diffusion of a single species through narrow pores, the influence of composition, and also geometrical factors such as tortuousity and porosity shall be included in the drag coefficient, i.e. $Đ_\mathrm{eff}$. The expression can therefore be simplified, noting that the porous material is stationary, $\mathbf{u}_2 = 0$:

$$-\boldsymbol{\nabla}\mu_1 = \frac{k_\mathrm{B}T}{Đ_\mathrm{eff}} \mathbf{u}_1 \; . \tag{10}$$

Therefore, extending to an expression of mass transport and dropping the subscripts for components, the expression is similar to Eq. 3 and Eq. 4:

$$\mathbf{J}^\mathrm{total} = \rho\mathbf{u} = -\frac{\rho}{k_\mathrm{B}T} Đ_\mathrm{eff} \boldsymbol{\nabla}\mu \; . \tag{11}$$

Furthermore, this appraoch allows a connection between the various transport coefficients:

$$D_\mathrm{t} = L\frac{k_\mathrm{B}T}{\rho}\Gamma = D_0\Gamma = Đ_\mathrm{eff}\Gamma \tag{12}$$

2.2.1 Non-equilibrium simulation techniques

Since diffusion is a process that is invoked by a departure from equilibrium, a multitude of different approaches has been devised, of which the majority drive the system of interest away from equilibrium. These approaches frequently mimic a real experiment in order to link observation from simulation with phenomenological transport properties. Transient methods are a telling example for this notion. The Gradient Relaxation Molecular Dynamics (GRMD) method was introduced by Maginn et al. [9] to study mass transport in zeolites. The approach determines the diffusivity by monitoring the time-dependent recurrence of a non-equilibrium system to a state of equilibrium. More specifically, a step profile in the density of a fluid in zeolite cages was imposed and used as a starting point for a transient MD simulation. Diffusive mass transport causes the density profile to smoothly flatten out to a state of uniform density. The time evolution of the density profile is analysed and yields the diffusion coefficient. In another related approach, Salih [19] considered a simulation box of an equilibrated fluid in contact through a capillary with

---

[1] *Note (will not be submitted): the "Dusty Gas" approach deals with Maxwell-Stefan diffusion in pores and it yields (Krishna,1997):*

$$\frac{x_1'}{RT}\boldsymbol{\nabla}\mu_1'\Big|_{T,p} - \frac{1}{c_\mathrm{t}' RT}\left[(c_1\bar{v}_1 - \omega_1')\,\boldsymbol{\nabla}p' - \omega_1' c_2 F_2\right] = \frac{x_2' N1}{c_\mathrm{t}' Đ_{12}'}$$

Long story short, it's a very complicated and elaborate approach with plenty of assumptions for the species, most notably that the porous material is distributed equally in our system, which is obviously not the case for the slit pore.

a vacuum space. The expansion in monitored and the time evolution in density is related to the analytical solution to obtain the diffusion coefficient. Surely, many similar computer experiments of this transient nature could be envisioned to calculate the diffusivity. The principal difficulty of this methodology, however, lies in determining whether the simulation occurs in the linear response regime as well as in limitations of the statistical reliability.

Another subcategory of the non-equilibrium techniques are methods to simulate a non-equilibrium system in a steady state. Heffelfinger and Swol proposed the Dual Control Volume Grand Canonical Molecular Dynamics (DCV-GCMD) method [20] in an attempt to directly simulate diffusive flux triggered by a gradient in chemical potential and in the absence of a pressure gradient. To this end, an elongated simulation box is divided into three relevant compartments. Reservoir compartments are located at the right and left end of the system and the flow region is located in the center, between the two reservoirs. Each reservoir is kept at a constant chemical potential by inserting and deleting particles from the reservoir. In one implementation, the simulated fluid is composed of two species that only differ in colour. By keeping high and low chemical potential regions for the two species on opposite sites of the simulation box, the overall system is kept at constant density. In other instances [18], a single component fluid is simulated and imposing a difference in chemical potential leads to one reservoir being at a higher pressure than the other, which in turn makes a net flux occur in the flow region. The DCV-GCMD method has the advantage that it is evident whether a simulation happens in the linear response regime or not. While the steady state nature of the simulation allows for an improved accumulation of statistics, the combination of stochastic and deterministic elements poses a challenge for two reasons [21]. First, inserted particles must be assigned a velocity that matches the average streaming velocity, which in turn is not known a priori. Second, the insertion and deletion of particles alters the dynamics of the molecules and the number of insertion or deletion events has an influence on the mass transport.

Last but not least, the External Field Non-Equilibrium MD (EF-NEMD) method has been one of the first methods introduced [14], although wide spread use of this method was hindered by limitations in computational power as the systems studied usually need to be relatively large to yield reliable results. The approach itself is very straight forward. An equilibrated molecular dynamics sample is taken out of equilibrium with an external force field acting on all or part of the fluid particles. The external field invokes additional acceleration into a specific direction, invoking a macroscopic flux in the same direction. For a small perturbation, it is common to regard this external force field equivalent to a chemical potential or a pressure gradient. It can be compared to gravity homogeneously acting on all particles of the sample. However, the external field is an extension to the Hamiltonian of the ensemble [22], and thus, it has an effect on the interaction between particles. The effect might not be negligible in some cases, in particular, when considering the interaction between fluid and wall particles. Moreover, some reservation to the EF-NEMD method are targeted towards the fact that it has not been formally demonstrated under what conditions the equivalence of external field and chemical potential gradient is justified and when the assumption breaks down [21]. Nonetheless, more recent publications indicate that the method yields good results and shows greater potential for an extension to more complex systems [17].

In light of this background, the objective of the following sections is to present a novel implementation of the EF-NEMD approach and evaluate it in the context of the theoretical framework presented in the beginning of this section. It is intended to make the methodology more applicable to study transport phenomenon in porous structures.

3 Non-Equilibrium Molecular Dynamics Simulations

For the investigation of diffusion on the nanoscale, it is necessary to model the substances on a molecular level. Molecular Dynamics simulation is the method of choice for the computation of dynamic properties on the nanoscale because it has decisive advantages over Monte Carlo

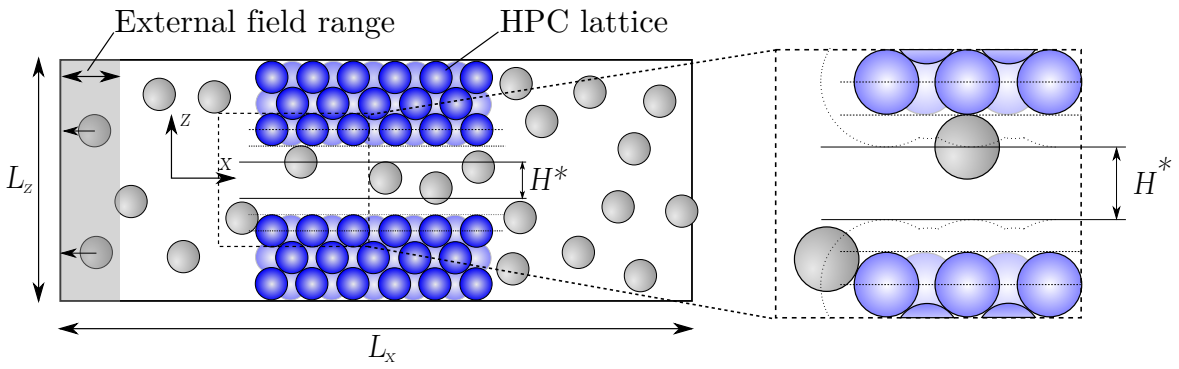

Figure 1. Schematic representation of the slit pore geometry. Blue spheres represent the particles of a porous solid. Gray spheres are fluid particles. Periodic boundary conditions are applied in all directions. A close-up of the slit pore channel and the definition of the pore width are also shown. The volume accessible to the fluid is schematically depicted by the dotted line. The y direction (in plane) is not shown.

methods [6], particularly for complex molecules and liquid-like densities. A realistic production of the molecular trajectories is quintessential to the calculation of transport properties.

The Molecular Dynamics scheme is enhanced by the application of an external force in order to drive the system away from equilibrium and to a steady-state. As it was outlined in section 2, the application of an external force has numerous advantages over the other commonly applied methods. Above all, it generally improves over other methods in efficiency, i.e. computational effort, for systems of comparable sizes [21]. Moreover, the method is purely deterministic, meaning that the molecular trajectories are not influenced by any stochastic elements that could alter the system's dynamics, such as the random insertion of particles. Thus, there is no obstacle to apply the approach to a plenitude of applications, for example to complex geometries of the porous material or to chain-like molecules such as polymers.

The novel aspect of this NEMD implementation is the fact that the external field is only applied to the particles which are in a thin slab at the boundary of the simulation box. Consequentially, the dynamics of the particles are only altered in a small section of the simulation box and the main interaction between fluid and pore structure is not affected by the external perturbation. However, due to the fact that the external field acts on only a small region of the simulation box, the density in the pore is not uniform. The implications and results are thoroughly discussed in section 4. The following section will elucidate the specifics of the simulation method.

3.1 *System setup and force fields*

A slit pore is a simple geometrical structure lending itself for the study of fluid dynamics and mass transport phenomena due to its clearly laid out characteristics. At a steady state, a Poiseuille-like flow develops in a slit pore when a fluid is forced through the pore. The slit pore geometry has been subject of considerable interest in the molecular modeling community [23–25]. Thus, the porous material is arranged as a slit pore in this study.

The definition of the geometry used in this work is shown in Fig. 3.1. The wall is constructed using a hexagonal closed packing lattice. The particles are tethered to their lattice positions using a spring of the form:

$$U_i^{\text{latt}} = k_{\text{s}}(\mathbf{r}_i - \mathbf{r}_i^0)^2 \,, \tag{13}$$

where k_{s} is the spring constant, $\mathbf{r}_i$ is the position of the particle i in the wall with respect to its lattice position, $\mathbf{r}_i^0$.

For modeling the fluid, in turn, a single-center Lennard-Jones (LJ) potential was used. More

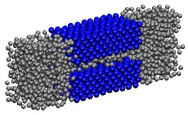

(a) Small realization of the narrow pore system with a pore width of $H^* = 1.5\sigma$ and a pore length of $\Delta L_x = 9.3\sigma$.

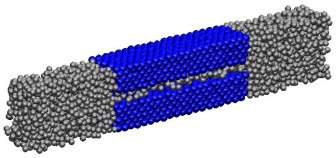

(b) Large realization of the narrow pore system with a pore width of $H^* = 1.5\sigma$ and a pore length of $\Delta L_x = 18.3\sigma$.

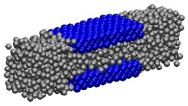

(c) Small realization of the wide pore system with a pore width of $H^* = 4.0\sigma$ and a system height of $L_z = 13.1\sigma$.

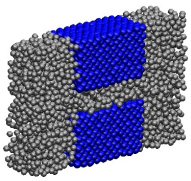

(d) Large realization of the wide pore system with a pore width of $H^* = 4.0\sigma$ and a system height of $L_z = 26.1\sigma$.

Figure 2. Snapshots of the four different model systems for the narrow and wide pore that were investigated in this study. Details about the setup of each system are given in Table 3.1

specifically, the fluid-fluid interactions are given by the LJ cut and shifted potential [26],

$$U_{ij}^{\mathrm{LJ}}(r_{ij}) = \begin{cases} 4\epsilon_{ij}\left[\left(\frac{\sigma_{ij}}{r_{ij}}\right)^{12} - \left(\frac{\sigma_{ij}}{r_{ij}}\right)^{6} - \left(\frac{\sigma_{ij}}{r_{ij}^{\mathrm{c}}}\right)^{12} + \left(\frac{\sigma_{ij}}{r_{ij}^{\mathrm{c}}}\right)^{6}\right] & r_{ij} < r_{ij}^{\mathrm{c}}\ , \\ 0 & r_{ij} \geq r_{ij}^{\mathrm{c}} \end{cases} \tag{14}$$

where σ_{ij} and ϵ_{ij} are the size and energy parameters of the LJ potential, r_{ij} is the distance between particles i and j, and r_{ij}^{c} is the distance at which the potential between particles i and j is truncated. σ is commonly referred to as the molecular diameter. The cut-off distance of the Lennard-Jones potential was chosen to be 2.5σ. For the solid-solid and fluid-solid interactions a purely repulsive potential, the Weeks-Chandler-Andersen (WCA) potential, was used [27]. The WCA potential is a cut and shifted Lennard-Jones potential with a cut-off radius $r_{ij}^{\mathrm{c}} = 2^{1/6}$.

Two different values for the pore width were realized in order to shed light on the influence of various combinations of system parameters. Namely, a narrow pore with a pore width $H^* = 1.5\sigma$ and a wide pore with $H^* = 4.0\sigma$, as shown in Figure 2. A brief discussion on defining the pore width is given below. For each of the two pore sizes, a smaller system and a larger system was under investigation. While the system of the narrow pore was stretched along the length of the slit pore in the x direction, the system of the wide pore was enlarged perpendicular to the pore in the z direction by adding more layers of wall molecules. The details of the systems' geometry are given in Table 3.1.

The mass transport through the slit pore is studied using non-equilibrium molecular dynamics. The fluid flow is induced applying a gravity-like external field of the form $f_{\mathrm{ex}} = -m_i g\hat{\mathbf{x}}$, where m_i is the mass of particle i, g is the magnitude of the external field, and $\hat{\mathbf{x}}$ is the unit vector along the x direction, i.e. in the direction of the flow. This external field is only applied in an small region of the system (see the shaded region in Fig. 3.1) in order to induce the flow with the minimal perturbation to the system. The field acts in negative x direction at the left boundary of the simulation box and the thin slab in which it is applied is three molecular diameters thick. Periodic boundaries apply in all three dimensions, meaning that a particle that exits the

Table 1. Different pore geometries and the respective number of particles in each simulation setup. The volume accessible to the fluid is estimated by subtracting a box-shaped sections for the wall structure (see section 3.2 for details). Porosity is meant as a measure on how much wall surface the fluid faces.

Pore size H^* $[\sigma]$	1.504	1.504	4.004	4.004
Dimensions of the simulation box $[\sigma]$				
Simulation box length L_x	40.000	80.000	40.000	40.000
Simulation box depth L_y	8.736	8.736	8.736	8.736
Simulation box height L_z	13.113	13.113	10.371	26.096
Number of wall molecules	1200	2400	600	2400
Number of fluid molecules	1490	2958	1412	2982
Est. volume accessible to fluid $[\sigma^3]$	2695.9	5506.1	2589.5	5529.5
Corresponding density $[1/\sigma^3]$	0.553	0.537	0.545	0.539
Porosity H^*/L_z	0.115	0.115	0.386	0.153

simulation box at one end is re-inserted at the opposite boundary [28].

3.2 *Definition of the pore geometry*

Simulations for two different pore widths are under consideration. The narrow system exhibits a pore width of 1.5σ, while a pore width of 4 molecular diameters was chosen for the wider system. The slit pore lies symmetrically in the center of the simulation box. The pore has a length of 9.3 and 18.3 molecular diameters for the three short and the long systems, respectively. For soft-sphere molecules, such as the LJ fluid and the WCA wall, the pore width and length cannot be defined unambiguously. For the following discussion, the pore width shall be defined as the distance between the center of mass of the inner-most wall layer less 2 molecular diameters as outlined in Fig. 3.1. This would be the width that the hard-sphere fluid could access within the pore. An unambiguous definition of the pore width is not possible and other definitions can be found in the literature [24], but for a densely packed pore material and a dense fluid within, the definition chosen in this case seems more appropriate. With greater surface roughness, i.e. more spacing between the lattice positions of the wall molecules, and thus more volume accessible inside the pore, it might be necessary to find a different definition of the pore width. Naturally, these effects also have an effect on the overall volume accessible to the fluid. From the entire simulation box volume, the volume of the pore material and the inaccessible volume must be subtracted. The values given for the volume accessible to the fluid in Table 3.1 are close estimates for the actual accessible volume, because smooth edges of the pore wall were not explicitly taken into account.

3.3 *Molecular simulation details*

Since the external field does a certain amount of work on the system which later must be dissipated as heat, the temperature of the system must be controlled by a thermostat. A Gaussian thermostat, i.e. an isokinetic thermostat, is applied only to the particles belonging to the wall. Thus, the heat generated in the fluid is removed from the system via the wall structure by the interaction between the wall and the fluid. This leaves the motion of the fluid molecules unaltered.

The equations of motion for the particles in the wall are given by:

$$\begin{aligned} \frac{\mathrm{d}\mathbf{r}_i(t)}{\mathrm{d}t} &= \mathbf{v}_i(t), \\ \frac{\mathrm{d}\mathbf{v}_i(t)}{\mathrm{d}t} &= \frac{\mathbf{f}_i(t)}{m_i} - \chi(t)\mathbf{v}_i(t), \end{aligned} \tag{15}$$

subject to the constraint:

$$\frac{\mathrm{d}\mathcal{T}(t)}{\mathrm{d}t} = \frac{\mathrm{d}}{\mathrm{d}t}\left(\frac{1}{k_\mathrm{B}N_\mathrm{dof}}\sum_{i=1}^{N_\mathrm{w}} m_i\mathbf{v}_i(t)\cdot\mathbf{v}_i(t)\right) = 0\ , \tag{16}$$

where $\mathbf{v}_i(t)$ and $\mathbf{f}_i(t)$ denote the velocity and total force of particles i, respectively, k_B is the Boltzmann's constant, N_w is the total number of particles of the wall, and N_dof is the number of degrees of freedom. The parameter $\chi(t)$ in Eq. 15 is a friction coefficient that guarantees a constant kinetic temperature, $\mathcal{T}$. The equations of motion are integrated using the leap-frog algorithm [29]. The fluid particles are not subject to any thermostat and the equations of motion that govern their dynamics are the same as in Eq. 15 setting $\chi(t) = 0$ at every time step. To achieve an increase in computational efficiency, a Verlet list of closest neighbors is employed when calculating the forces for each time step [22]. The list sphere radius was chosen to be 1.0σ.

In this work, thermodynamic and structural properties are expressed in reduced variables for temperature, density, and time. The quantities are defined as $T^* = k_\mathrm{B}T/\epsilon$, $\rho^* = N_\mathrm{f}\sigma^3/V$ and $t^* = t\sqrt{(m\epsilon/\sigma^2)}$. The LJ parameters and m, which represents the molecular weight, can be used to express all other units of interest.

The central observable when investigating mass transport phenomena is the molecular flux. The flux in x direction can be directly measured by counting the number of molecules crossing the $x = 0$ plane in a certain amount of time in relation to the accessible area in the xy plane A_{yz},

$$J_i = \frac{N_i^+ - N_i^-}{t_\mathrm{run}A_{yz}}\ , \tag{17}$$

where J_i denotes the molar flux of species i, N_i^+ and N_i^- denote the amount of molecules of species i which have passed the plane in the time t_run in positive and negative x direction, respectively.

Each system setup was equilibrated for 400 000 time steps with no external forces applied. Then, with the external field applied, simulations ran for 2.5 million time steps after an equilibration period of 250000 time steps. All simulations were performed at $T^* = 1.5$ and the time step was chosen to be $t^* = 0.01$, both given in reduced units. In order to avoid phase separation within the system, the temperature was chosen to be at a super-critical value, $T^* = 1.5$. The fluid densities are close to 0.5. The actual density of each system is not uniform and an average density can only be estimated from the number of molecules over the volume accessible to the fluid. The values for this estimate average density are given in Table 3.1. Several runs were performed for each state point to give a measure for the error to be expected from the simulations.

4 Results and Discussion

The dynamics of the mass transport greatly depend on the magnitude of the external field applied to the system. The response to the external field is also influenced by the architecture of the simulation. The impact of the perturbation on the mechanical and thermal equilibrium and the results for the different systems shown in Figure 2 are given and discussed in the following section. In particular, the density distribution, the kinetic temperature and the average particle velocities were investigated closely and the respective measures, which characterise a systems mass transport properties, such as effective diffusivities, were calculated. Finally, a discussion on simulating counter diffusion follows.

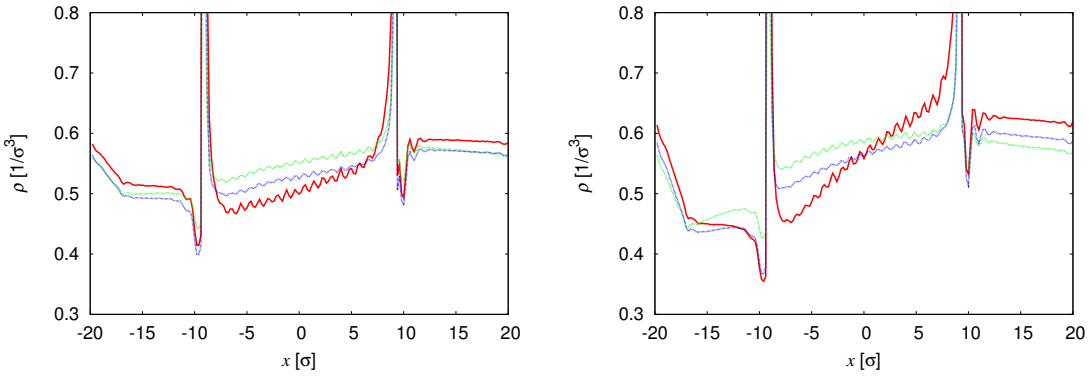

(a) (b)

Figure 3. Selected density profiles along the length of the simulation box, i.e. in x direction. On the left, (a), it is $f_{\text{ex}} = 0.2\frac{\epsilon}{\sigma}$. The figure on the right (b) shows $f_{\text{ex}} = 0.5\frac{\epsilon}{\sigma}$. Solid red lines represent the profile for the small realization of the narrow pore. Blue and green lines depict the small and large realization of the wide pore, respectively.

4.1 *Unidirectional mass transport*

Due to the application of the external field, the density is not uniform in the entire system. The external force, acting in the negative x direction, builds up a pressurized bulk on the right of the porous structure, provoking an increase in density in the right bulk region. The fluid is squeezed into the porous structure and a planar Poiseuille-like flow develops in the slit-pore. While the density in the bulk region is uniform for a moderate perturbation, a linear density gradient develops within the pore. In order to quantify the differences in density, the density distribution along the length of the pore was measured. To this end, the simulation box was divided into thin slabs. For each slab, the average amount of molecules was measured during the simulation and a density profile along the x direction, the direction of flow, could be obtained. Moreover, to assess the heat transport within the system, the kinetic temperature was measured in the same fashion.

Density profiles of three exemplary cases in terms of system geometry are shown in Fig. 3 for $f_{\text{ex}} = 0.2$ and $0.5\frac{\epsilon}{\sigma}$. Density profiles for all other conditions can be taken from the supplementary material.

It can be seen in Fig. 3 that the density profile inside the pore shows a regular undulation pattern. These undulations can be attributed to the uneven topology of the pore surface. The issue is related to the fact that it is not possible to define an unambiguous pore size, mentioned in section 3.2. Since the slit pore is a structured wall consisting of soft spheres, the surface of the slit pore is not flat but has a smooth and wavy surface. The fluid has more space to expand where there are dents in pore surface. What is more, the wall molecules are not still. They rather vibrate about their lattice positions. The roughness of the pore surface was not explicitly taken into account when the density profile was calculated. Luckily, this feature does not hinder the analysis of the simulations since average values along the pore are considered.

With a pore width of $H^* = 4.0\sigma$, the structure of the confined fluid within the pore is different from a narrow pore [24], which can be seen in Fig. 4. Two dense layers develop similar to the narrow pore. In the center of the pore, the fluid has considerably more space and resembles a bulk fluid, which implies that the fluid exhibits a higher mobility.

With the slit pore being in direct contact with the bulk fluid, two particular phenomena must be kept in mind. The transition from bulk to confined fluid leads to certain entrance and exit effects. Particularly in the high-density bulk phase, a layering in front of the pore takes place. The layering is similar to the layering taking place inside the slit pore and is due to the repulsive nature of the pore. These phenomena will have an effect on the mass transport. Naturally, the smaller systems are more prone to these effects. The ratio of surface area to accessible fluid

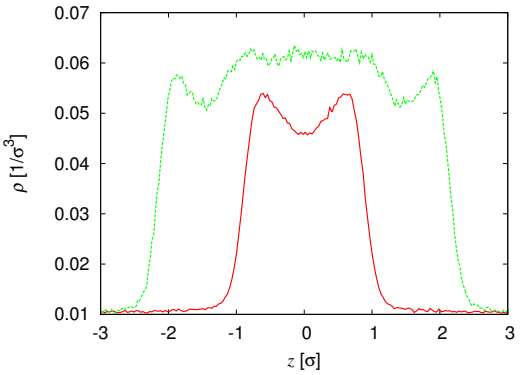

Figure 4. Density profile within the pore showing the structure of the fluid. The solid red line depicts the profile for the narrow pore while the dashed green lines shows the wide pore's profile.

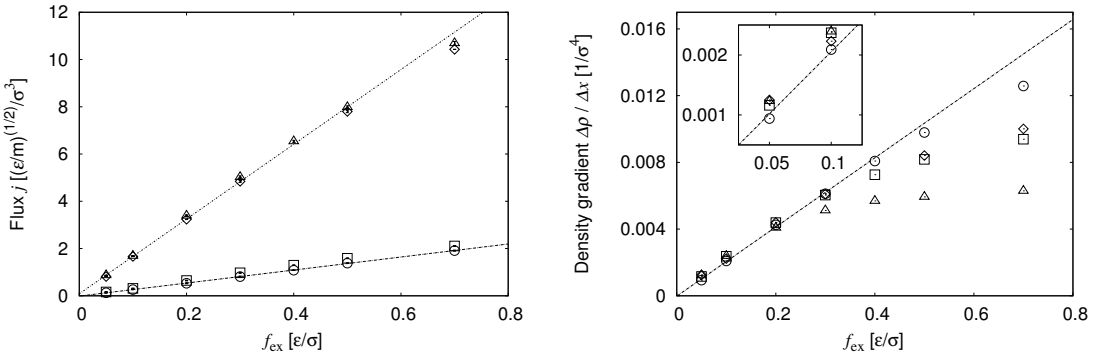

(a) Response of the molar flux.

(b) Response of the density gradient.

Figure 5. Influence of the external force field on the molar flux (a) and the density gradient (b). It is $\Delta\rho/\Delta x = (\rho_{\text{right}} - \rho_{\text{left}})/\Delta L_x$. Circles and squares represent the small and large realization of the narrow pore, triangles and diamonds the small and large realization of the wide pore, respectively. The straight dashed lines are a guide to the eye for a linear function.

volume is higher than for the small pores. For both pore sizes, we more than double the accessible volume for the bigger systems but only increase the surface area by roughly 60%.

Measuring the density in the bulk regions is an uncomplicated task as the available volume in these regions is correctly defined. However, the density within the pore is subject to the complications in defining the pore width. Furthermore, at the entrance and exit of the pore, the available volume changes in a continuous fashion, going from bulk to confinement. This point transition was not explicitly taken into account in the density profiles, as it creates the spikes in the profiles. The spikes are located at the entrance and exit of the slit pore. The average density in the bulk sections was taken from the simulations from which the difference in density could be calculated. Figure 3(a) shows that a weak external force invokes a linear response in the density distribution. The bulk densities are constant and the density gradient inside the pore is linear. The density gradient and the difference in bulk densities increase with the magnitude of the external field. As depicted in Fig. 3(b), the response is non-linear for larger magnitudes of external force field, depending on the system setup. The gradient inside the pore deviates from a linear gradient and for the large system, even the bulk density is not uniform. A similar conclusion can be derived from Figure 5(b). While the molar flux is linearly correlated to the external field, the increase in $\Delta\rho/\Delta x$ shows a growing deviation for high magnitudes of the force field.

For the small realization of the wide pore, the deviation of $\Delta\rho/\Delta x$ from a linear response is most prominent (triangles in Fig. 5(b)). It is obvious that the fluid faces less resistance from the porous structure compared to the other realizations because the ratio of the void area to the

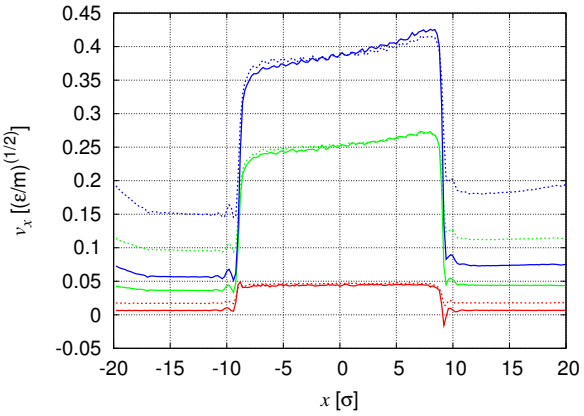

Figure 6. Average streaming velocity profile for the wide pore at two different porosities. Solid lines depict the system at low porosity (i.e. large realization in Fig. 2(d)) while dashed lines represent the results of the high porosity system (i.e. small realization in Fig. 2(c)). The profile for $f_{\text{ex}} = 0.05, 0.3$ and $0.5\frac{\epsilon}{\sigma}$ are plotted.

total area is much smaller than in the other cases. Porosity is given as a measure to evaluate this aspect and the values for each system's porosity are given in Table 3.1. By enlarging the system and adding porous structure in the z direction, the porosity is greatly reduced and larger bulk subsystem is created. As a consequence, the fluid cannot cross through the pore as easily.

The same effect can also be observed when looking at the average particle velocity in the flow direction. This reduction of porosity reduces the streaming velocity of the fluid in the bulk sections while the streaming velocity in the pore stays constant. As shown in Fig. 6, the bulk streaming velocity is more than halved by reducing the porosity from 0.386 to 0.153. Velocity profiles of the other system realizations can be found in the supplementary material.

Figure 7 shows the profile of the temperature in the system. It can be seen that heat transfer is strongly influenced by the system setup and the external forces applied. Since the system is observed in a steady state, there is an equilibrium between the energy added as a consequence of the action of the external force and the heat removed from the walls by the thermostat. The temperature profile in Figure 7 shows that the system is close to thermal equilibrium for a weak external field but far from it at an external forces of $0.5\frac{\epsilon}{\sigma}$. The profile also shows that heat is removed more easily from the small system and that the temperature increases considerably more for the large system at the same magnitude of f_{ex}. The temperature profile of the small realization of the wide pore (green lines in Fig. 7) indicates that it is increasingly important to monitor the fluid temperature when the porous structure makes up a small part of the system. Note that the thermostat is applied only at the walls, thus by adding porous material to the system, the heat transport can be facilitated. In opposition to this, strong external forces lead to a steady-state which is far from thermal equilibrium, as shown in Fig. 7(b). The heat transfer of the system can certainly be influenced by the interaction between fluid and wall particles. It seems logical that the motion of the wall molecules, and thus the spring constant k_{s} of the restoring force, must also have an influence. This however is not subject of this study and should be investigated in future research.

4.1.1 Effective diffusivities

The simulations yield a difference in density as well as the flux triggered by this density gradient. Equation 8 establishes the relationship between the flux and a gradient in density via the effective diffusion coefficient. With the bulk densities available from the simulations, the densities gradient can be expressed as:

$$\left(\frac{\Delta\rho}{\Delta x}\right) = \left(\frac{\rho_{\text{right}} - \rho_{\text{left}}}{\Delta L_x}\right) , \tag{18}$$

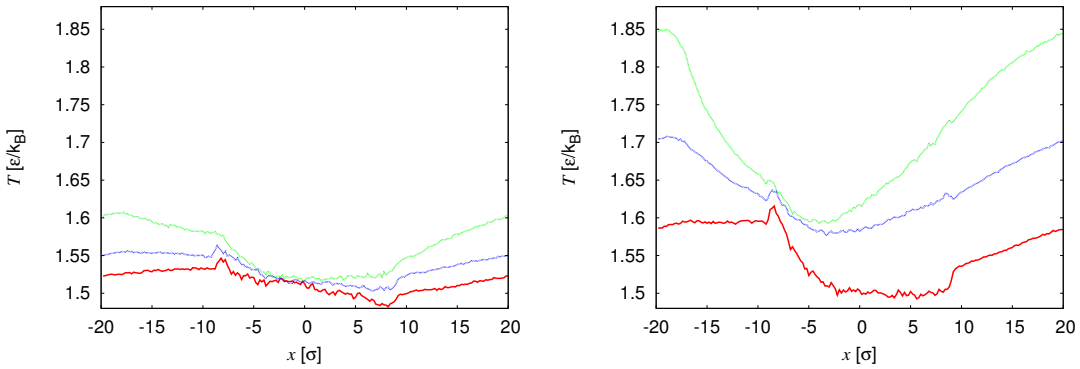

Figure 7. Selected temperature profiles along the length of the simulation box, i.e. in x direction. As for the density profiles in Fig. 3, (a) shows $f_{\mathrm{ex}} = 0.2\frac{\epsilon}{\sigma}$ and (b) shows $f_{\mathrm{ex}} = 0.5\frac{\epsilon}{\sigma}$. Solid red lines represent the small realization of the narrow pore, while blue and green lines depict the small and large realization of the wide pore, respectively.

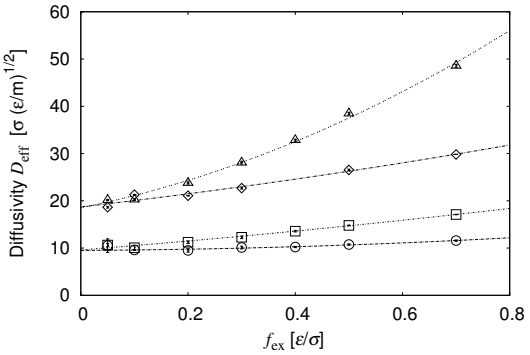

Figure 8. Effective diffusivities for the narrow and wide pore. As for Fig. 5, circles (small realization) and squares (large realization) denote the narrow pore system, triangles (small realization) and diamonds (large realization) denote the wide pore system. The dashed lines are a quadratic fit to the simulation results. Errors are estimated by running several runs for the same point. In most cases, the error bars are smaller than the symbols, though.

where ΔL_x is the length of the respective pore. Hence, the transport equation can be expressed as follows:

$$J_x \approx -D^{\mathrm{eff}} \left(\frac{\Delta\rho}{\Delta x}\right) . \tag{19}$$

The dependence of D^{eff} on the external force is plotted in Fig. 8. The figure shows that the effective diffusivity is not independent of the external field applied. As is expected, D^{eff} increases with the magnitude of the external field. Also, the results for the larger and the smaller system deviate from each other; as entrance effects play a larger role for the smaller system, a lower effective diffusion coefficient for the small system is expected. The figure also indicates that the coefficient approaches the same value as the external force approaches zero. Naturally, the error in the simulation increases as the observables also get closer to zero and are subject to larger fluctuations.

For the case that is under scrutiny here, the mass transport is not purely induced by a difference in chemical potential but also has a convective component to it. With an increasing density gradient, and therefore also an increasing pressure difference between the two bulk sections, this convective component also increases. The increase of the average fluid velocity v_x points to this as well. Thus, it can be argued that this convective component vanishes in the limit of $f_{\mathrm{ex}} \to 0$,

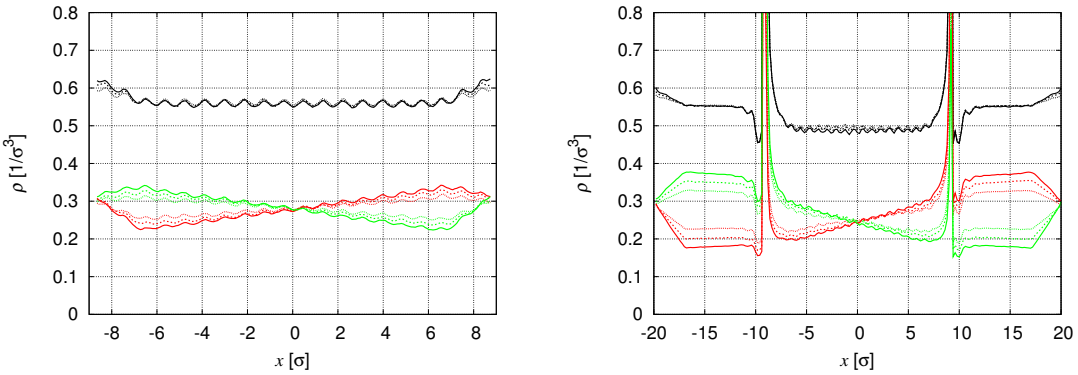

(a) System without bulk section.

(b) System with bulk section.

Figure 9. Counter diffusion in the narrow pore, $H^* = 1.5\sigma$.

and in this limit the effective diffusivity approaches the transport diffusivity D_t.

4.2 *Counter diffusion*

With the force applied in one specific direction, the fluid acquires momentum in the same direction and when reaching the steady state, a unidirectional flow develops in the system. What is more, the slit pore poses a resistance to the flow and creates a build up in density on one side. The system is therefore brought out of mechanical equilibrium and the mass flux measured has a certain convective contribution. To circumvent this issue, the homogeneous fluid can be artificially divided into equal parts of two species of different colour that otherwise have no distinction. Moreover, another force field is applied to the system on the opposite side of the simulation box and acting in the opposite direction, but only on one particular coloured species, while the other force field acts on the second species. The flow of one species is therefore countered by a flow of the other species. Pressure and density in the system can thus be maintained uniform and with the heat being rapidly removed from the system, it is also at a constant temperature. The only gradient in this system is a concentration gradient of the two species. The opposing force field distinguishes between the two species and separates them at the boundary. The mechanism "Avendaño demon" can be compared to a Maxwell demon that is able to reduces the entropy of the system [30]. Similar approaches to separate the colour-distinguished species involve the insertion and deletion of particles, such as the DCV-GCMD method [20], or a stochastic enhancement of the periodic boundary conditions under which some molecules would be reflected from the boundary according to a certain probability [31]. Counter-diffusion simulations for the small systems of the narrow and wide pore were simulated. The same systems as they are shown in Figure 2, and for each pore width, a system with a pore only, i.e. an infinite slit pore with no connecting bulk phases, were simulated. Fig. 9 depicts the density distribution along the x axis in a narrow slit pore with and without a bulk fluid region adjacent to the pore. It shows that the total density in the system is uniform except for the section where the opposing forces have been applied, where a slight increase in density is recorded. It stems from the opposing external fields that push the molecules into each other and provokes a slightly higher pressure, and therefore also a rise in density. In the central part of the simulation, the density is uniform and it can be concluded that the simulation is very close to a state of mechanical equilibrium. The distribution of the two colour-distinguished species of the fluid can also be taken from Fig. 9. The density gradients show a perfectly linear behaviour and the slope can be calculated from the profiles by fitting a linear function to the density distribution. The density gradient within the pore is more prominent than the gradient in the bulk sections, especially for the narrow pore.

The two species have opposing gradients of the same magnitude, which can be taken from

Table 2. Colour-counter NEMD results for the narrow pore as well as self-diffusivity for the confined fluid calculated from EMD. The number in the parantheses denotes the uncertainty in the last digit.

Pore width $H^* = 1.5$ without bulk section,			Average density $\overline{\rho} = 0.56$			
f_{ex}	J_1	J_2	$\frac{\mathrm{d}\rho_1}{\mathrm{d}x}$	$\frac{\mathrm{d}\rho_2}{\mathrm{d}x}$	$\mathcal{D}_1$	$\mathcal{D}_2$
0.2	-0.0015(4)	0.0021(3)	0.00444	-0.00429	0.34(9)	0.50(9)
0.3	-0.0029(3)	0.0025(2)	0.00636	-0.00642	0.45(4)	0.39(3)
0.4	-0.0036(3)	0.0036(5)	0.00837	-0.00835	0.43(2)	0.43(6)
$H^* = 1.5$, with bulk section $L_x = 40\sigma$,			Average density $\overline{\rho} = 0.57$			
0.2	-0.0018(6)	0.0021(6)	0.00411	-0.00428	0.5(2)	0.5(1)
0.3	-0.0030(3)	0.0031(5)	0.00580	-0.00586	0.53(6)	0.52(8)
0.4	-0.0041(5)	0.0041(6)	0.00781	-0.00775	0.52(6)	0.53(7)
Self-diffusivity in the xy plane from EMD at $\rho = 0.57$				$D_{\text{s},xy} = 0.508$		

Table 4.2 for the narrow pore and from Table 4.2 for the wide pore. The approach gives a similar picture to the density gradient in the DCV-GCMD approach [20], with a similar counter diffusion of colour-distinguished species of an otherwise homogeneous Lennard-Jones fluid. Along with the density gradients, the flux for each species is given in the same table for three different external field strengths. Based on this information, the diffusivity of the system can be calculated similar to the way it was calculated for the pressure-induced diffusion,

$$J_i = -\mathcal{D}_i \frac{\mathrm{d}\rho_i}{\mathrm{d}x} \,. \tag{20}$$

For the systems discussed in the previous section, the molecular flux happens predominantly in one direction only, due to the presence of a pressure difference, and the diffusion coefficient had a certain convective contribution to it. With the mechanical equilibrium restored by opposing forces acting each on the colour-distinguished species, the flux for each species is opposed to the other species' flux and these counter fluxes hinder the diffusion of each species mutually. The magnitude of the external force has an effect on the magnitude of the flux and the slope of the density gradient. It has no effect on the diffusion coefficients calculated with Eq. 20, though. Table 4.2 and 4.2 suggest that a higher force field is beneficial in this case, as the uncertainties for the calculation of the diffusion coefficient $\mathcal{D}_i$ decrease with a stronger force field. The resulting mass transport is an order of magnitude lower than in the case of unidirectional mass transport. Thus, the resulting mass transport coefficient is also an order of magnitude lower than the previously described effective diffusivity. In this special case, the diffusion coefficient $\mathcal{D}_i$, which is inherently different from the effective diffusion coefficient D_{eff}, was defined to account for this aspect. With only one type of fluid-fluid interaction present, a comparison to the self-diffusion coefficient is in order. The results for the self-diffusion coefficient of the confined fluid were independently calculated using EMD and are given in Table 4.2 and 4.2. It is important to note that the self-diffusion coefficients were calculated for the mobility in the xy plane, because the fluid is confined in the z direction and therefore the flux was only measured in the x direction.

The results are of same order of magnitude, but the self-diffusion coefficient indicates a slightly higher mobility of the particles than the results of the counter-diffusion simulations would suggest. It shall also be noted that the system with a bulk fluid compared to the pore-only system exhibit a higher diffusivity. For a reliable conclusion on the results of the counter diffusion simulation, it would be necessary to engage in further research, even though the results largely agree with the conclusions made in previous research on diffusivities from NEMD simulations [20]. In particular, an analysis of the density dependence of $\mathcal{D}_i$ would be necessary to conclude the nature of the diffusion coefficient.

Table 3. Colour-counter NEMD results for the wide pore as well as self-diffusivity for the confined fluid calculated from EMD. The number in the parentheses denotes the uncertainty in the last digit.

Pore width $H^* = 4.0$ without bulk section,			Average density $\overline{\rho} = 0.63$			
f_{ex}	j_1	j_2	$\frac{\mathrm{d}\rho_1}{\mathrm{d}x}$	$\frac{\mathrm{d}\rho_2}{\mathrm{d}x}$	$\mathcal{D}_1$	$\mathcal{D}_2$
0.2	-0.0012(3)	0.0013(3)	0.00336	-0.00344	0.37(9)	0.37(9)
0.3	-0.0020(2)	0.0018(2)	0.00489	-0.00494	0.40(3)	0.35(3)
0.4	-0.0025(3)	0.0023(3)	0.00657	-0.00669	0.39(4)	0.39(4)
$H^* = 4.0$, with bulk section $L_x = 40\sigma$,			Average density $\overline{\rho} = 0.55$			
0.2	-0.0018(6)	0.0021(6)	0.00411	-0.00428	0.5(2)	0.5(1)
0.3	-0.0030(3)	0.0031(5)	0.00580	-0.00586	0.53(6)	0.52(8)
0.4	-0.0041(5)	0.0041(6)	0.00781	-0.00775	0.52(6)	0.53(7)
Self-diffusivity in the xy plane from EMD at $\rho = 0.638$				$D_{\text{s},xy} = 0.308$		

5 Conclusion

With molecular simulation becoming a genuine alternative to classical modeling, the simulation of mass transport on the nanoscale calls for highly efficient and versatile simulation methods. In this study, a novel approach of a NEMD simulation scheme was presented. Its core features adhere to several practical principles and through a combination of several advantages over existing methods, the approach appears to be superior by circumventing previously encountered difficulties. Namely, the approach is purely deterministic. Therefore, the methodology is not prone to any undesired effects due to the combination of stochastic and deterministic elements. Moreover, the particle dynamics are unaltered in the critical transport region because the artificial perturbation is only applied in a thin slab of the simulation box. The perturbation on the system can be arbitrarily small, enabling steady-state simulations very close to equilibrium conditions. Also, only the molecules making up the porous material are subject to a Gaussian thermostat and ensure that heat from dissipation is removed from the system.

It shall be noted that the approach is not limited to simple systems, albeit demonstrated on an idealized model in this study. Existing codes for molecular simulation can easily be enhanced to incorporate the approach and it can be used to simulate elaborate models of industrial fluids or very complex geometries of the porous structures. Promising development can be envisioned in this respect. Also, there is potential in further investigating the system's response in terms of its pressure profile. Naturally, the approach can be refined to compute additional transport properties such as momentum transport, i.e. fluid viscosity or heat transport. Such a refinement would allow further validation of the calculated properties. Above all, it will be necessary to apply the methodology to more realistic systems by using interaction potentials of real fluids and explore the modeling of complex porous materials.

References

[1] J. Goldsmith and C.C. Martens, *Molecular dynamics simulation of salt rejection in model surface-modified nanopores*, The Journal of Physical Chemistry Letters 1 (2010), pp. 528–535.

[2] K.P. Travis, B.D. Todd, and D.J. Evans, *Departure from Navier-Stokes hydrodynamics in confined liquids*, Physical Review E 55 (1997), pp. 4288–4295.

[3] W. Bowen and J. Welfoot, *Predictive modelling of nanofiltration: Membrane specification and process optimisation*, Desalination 147 (2002), pp. 197–203.

[4] J.K. Holt, H.G. Park, Y. Wang, M. Stadermann, A.B. Artyukhin, C.P. Grigoropoulos, A. Noy, and O. Bakajin, *Fast mass transport through sub-2-nanometer carbon nanotubes*, Science 312 (2006), pp. 1034–1037.

[5] K.E. Gubbins, Y. Liu, J.D. Moore, and J.C. Palmer, *The role of molecular modeling in confined systems: impact and prospects*, Physical Chemistry Chemical Physics 13 (2011), p. 58.

[6] E.J. Maginn and J.R. Elliott, *Historical perspective and current outlook for Molecular Dynamics as a chemical engineering tool*, Industrial & Engineering Chemistry Research 49 (2010), pp. 3059–3078.

[7] D.N. Theodorou, *Progress and Outlook in Monte Carlo Simulations*, Industrial & Engineering Chemistry Research 49 (2010), pp. 3047–3058.

[8] A. Einstein, *Über die von der molekularkinetischen Theorie der Wärme geforderte Bewegung von in ruhenden Flüssigkeiten suspendierten Teilchen*, Annalen der Physik 322 (1905), pp. 549–560.

[9] E.J. Maginn, A.T. Bell, and D.N. Theodorou, *Transport diffusivity of methane in silicalite from equilibrium and nonequilibrium simulations*, The Journal of Physical Chemistry 97 (1993), pp. 4173–4181.
[10] P.M. Chaikin and T.C. Lubensky Cambridge University Press, New York, USA, 1995.
[11] R. Kubo, *Statistical-Mechanical Theory of Irreversible Processes. I. General theory and simple applications to magnetic and conduction problems*, Journal of the Physical Society of Japan 12 (1957), pp. 570–586.
[12] S. Bhatia and D. Nicholson, *Hydrodynamic origin of diffusion in nanopores*, Physical Review Letters 90 (2003), p. 016105.
[13] D. Nicholson, *The transport of adsorbate mixtures in porous materials: Basic equations for pores with simple geometry*, Journal of Membrane Science 129 (1997), pp. 209–219.
[14] D. Evans and O. Morriss, *Non-Newtonian molecular dynamics*, Computer Physics Reports 1 (1984), pp. 297–343.
[15] R.B. Bird, W.E. Stewart, and E.N. Lightfoot 2nd ed., Jon Wiley & Sons, New York, USA, 2002.
[16] E.L. Cussler 3rd ed., Cambridge University Press, New York, USA, 2009.
[17] S. Chempath, R. Krishna, and R.Q. Snurr, *Non-equilibrium molecular dynamics simulations of diffusion of binary mixtures containing short n-alkanes in faujasite*, Journal of Physical Chemistry B 108 (2004), pp. 13481–13491.
[18] K. Travis and K. Gubbins, *Combined diffusive and viscous transport of methane in a carbon slit pore*, Molecular Simulation 25 (2000), pp. 209–227.
[19] A. Salih, *Molecular Simulation of the Adsorption and Transport Properties of Carbon Dioxide, Methane, Water and their Mixtures in Coal-like Structures*, Ph.D. diss., Imperial College London, London, UK, 2010.
[20] G.S. Heffelfinger and F. Swolvan , *Diffusion in Lennard-Jones fluids using dual control volume grand canonical molecular dynamics simulation (DCV-GCMD)*, Journal of Chemical Physics 100 (1994), p. 7548.
[21] G. Arya, H.C. Chang, and E.J. Maginn, *A critical comparison of equilibrium, non-equilibrium and boundary-driven molecular dynamics techniques for studying transport in microporous materials*, Journal of Chemical Physics 115 (2001), pp. 8112–8124.
[22] M. Allen and D. Tildesley Oxford University Press, Oxford, UK, 1987.
[23] Q. Cai, M.J. Biggs, and N.A. Seaton, *Effect of pore wall model on prediction of diffusion coefficients for graphitic slit pores*, Physical Chemistry Chemical Physics 10 (2008), pp. 2519–2527.
[24] K.P. Travis and K.E. Gubbins, *Poiseuille flow of Lennard-Jones fluids in narrow slit pores*, The Journal of Chemical Physics 112 (2000), p. 1984.
[25] R. Cracknell, D. Nicholson, and N. Quirke, *Direct molecular dynamics simulation of flow down a chemical potential gradient in a slit-shaped micropore*, Physical Review Letters 74 (1995), pp. 2463–2466.
[26] J. Vrabec, G.K. Kedia, G. Fuchs, and H. Hasse, *Comprehensive study of the vapourliquid coexistence of the truncated and shifted LennardJones fluid including planar and spherical interface properties*, Molecular Physics 104 (2006), pp. 1509–1527.
[27] J.D. Weeks, D. Chandler, and H.C. Andersen, *Role of repulsive forces in determining the equilibrium structure of simple liquids*, The Journal of Chemical Physics 54 (1971), p. 5237.
[28] D. Frenkel and B. Smit 2nd ed., Academic Press, London, UK, 1996.
[29] D. Brown and J. Clarke, *A comparison of constant energy, constant temperature and constant pressure ensembles in molecular dynamics simulations of atomic liquids*, Molecular Physics 51 (1984), pp. 1243–1252.
[30] W. Thomson, *The Sorting Demon Of Maxwell*, in *Proceedings of the Royal Institution*, Vol. 9, 1879.
[31] J.R. Whitman, G.L. Aranovich, and M.D. Donohue, *Thermodynamic driving force for diffusion: Comparison between theory and simulation*, The Journal of Chemical Physics 134 (2011), p. 094303.